

Optimization and scaling-up of porous solid electrolyte electrochemical reactors for hydrogen peroxide electrosynthesis

Received: 16 August 2024

Accepted: 20 March 2025

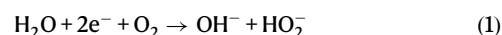
Published online: 04 April 2025

Erzhuo Zhao^{1,2,3}, Yixin Zhang¹, Juhong Zhan¹, Guangsen Xia⁴, Gang Yu^{1,5} & Yujue Wang^{1,2,3}✉

The recently developed porous solid electrolyte (PSE) reactor for electro-synthesis of hydrogen peroxide (H₂O₂) has attracted significant global interest. However, scaling up the PSE reactor for practical applications poses challenges, particularly due to performance decline in enlarged reactors. Here we systematically investigate how factors such as material selection, assembly parameters, flow field patterns, and operating conditions influence H₂O₂ electrosynthesis in the PSE reactor. Our findings reveal that the performance decline during reactor scale-up is primarily caused by the uneven flow field in the PSE layer. Based on these insights, we optimize the reactor design and develop a 12-unit modular electrode stack PSE reactor with a total electrode area of 1200 cm². The scaled-up reactor maintains efficient H₂O₂ electro-synthesis without significant performance decline. It operates stably for over 400 h and can produce up to 2.5 kg pure H₂O₂ (~83 kg 3% H₂O₂ solutions) per day with considerably lower energy costs (0.2–0.8 USD/kg H₂O₂) than the market prices of H₂O₂ stocks. This work represents a crucial advancement in the development of PSE reactor technology for practical H₂O₂ electrosynthesis.

Hydrogen peroxide (H₂O₂) is one of the 100 most important chemicals in the world and is widely used in numerous industrial and household applications, such as chemical synthesis, pulp and textile bleaching, water treatment, and disinfection^{1–4}. Currently, H₂O₂ is industrially produced by the anthraquinone process and commercially available as typically ~30–70 wt% aqueous solutions⁵. However, the anthraquinone process is an environmentally unfriendly and energy-intensive process that does not meet the needs of sustainable and low-carbon development. Moreover, the risks associated with the transport and storage of concentrated H₂O₂ stocks (e.g., explosion) have restrained the use of H₂O₂ in many applications, e.g., decentralized water and wastewater treatment⁶. In this context, electrosynthesis of H₂O₂ from two-electron (2e[−]) oxygen reduction reaction (ORR, Eqs. 1 and 2) has attracted

increasing attention worldwide because this approach may offer a more energy-efficient, low-carbon, and safer route for H₂O₂ production, especially for on-site H₂O₂ production in point-of-use applications^{6,7}.



Electrosynthesis of H₂O₂ is conventionally conducted in aqueous electrolytes with dissolved ions being the ion conductors. In case the water matrix has insufficient conductivity (e.g., freshwater and tap

¹School of Environment, Tsinghua University, Beijing, China. ²State Key Joint Laboratory of Environmental Simulation and Pollution Control, Tsinghua University, Beijing, China. ³Beijing Key Laboratory for Emerging Organic Contaminants Control, Tsinghua University, Beijing, China. ⁴Institute of Oceanographic Instrumentation, Qilu University of Technology (Shandong Academy of Sciences), Qingdao, China. ⁵Advanced Interdisciplinary Institute of Environment and Ecology, Beijing Normal University, Zhuhai, China. ✉e-mail: wangyujue@tsinghua.edu.cn

water), salt-based electrolytes (e.g., sodium sulfate and sodium chloride) are often added as the supporting electrolyte. The addition of salts can increase the cost of H_2O_2 electrosynthesis substantially⁸. Moreover, the presence of salts in the produced H_2O_2 solutions can considerably hamper their usability in some applications, and may thus require further separation and purification. To avoid the use of salt-based liquid electrolytes, Xia and co-workers developed an electrochemical reactor with porous solid electrolytes (PSEs) for H_2O_2 production⁹. As illustrated in SI Fig. S1, the PSE reactor consists of a carbon-based gas diffusion electrode (GDE) and iridium oxide (IrO_2) electrode as the cathode and anode for ORR and oxygen evolution reaction (OER), respectively. The anode and cathode sandwich a proton exchange membrane (PEM), a thin layer of PSE microspheres, and an anion exchange membrane (AEM), which allows H^+ and HO_2^- formed at the anode and cathode to transport and recombine to yield H_2O_2 in the middle PSE layer. A deionized (DI) water stream flowing through the PSE layer can then dissolve the pure H_2O_2 to produce H_2O_2 solutions without ionic impurities. Thus, by feeding the PSE reactor with oxygen/air and DI water, pure H_2O_2 solutions can be directly electrosynthesized for versatile uses⁹.

While the PSE reactor has shown great promise for H_2O_2 electrosynthesis, it still needs systematic evaluations and improvements to be applied in the field^{7,10,11}. For practical applications, the stability, scalability, and safety of electrochemical reactors are of paramount importance. However, to date, no studies have evaluated the long-term stability of the PSE reactor. Although some studies have shown that the PSE reactor can be stably operated for 100–200 h under 30 mA/cm^2 ^{29,12}, the long-term stability of PSE reactors under industrially relevant conditions remains unclear as it may take longer time and/or higher current densities for the decay of reactor components (e.g., GDE and membranes) to become appreciable^{8,13}. Moreover, the previous study showed that the performance of H_2O_2 electrosynthesis declined seriously as the PSE reactor was scaled up: as the electrode area of the PSE reactor was enlarged from 4 to 80 cm^2 , the cell voltage increased significantly and the Faradaic efficiency (FE) of H_2O_2 electrosynthesis decreased substantially⁹. Yet, the causes for the declined performance have not been well understood. Furthermore, sulfuric acid solutions are currently used as the anolyte in the PSE reactor^{9,11}, which is undesired in some scenarios (e.g., household applications) due to the safety concern. Overall, the above information highlights that there are still some issues and challenges that need to be resolved and overcome for scaling up and transferring the PSE reactor to practical applications.

The main objectives of this study were (i) to investigate the long-term stability and possible decay mechanism of PSE reactor during H_2O_2 electrosynthesis under industrially relevant conditions, (ii) to reveal the causes for the declined performance of enlarged PSE

reactors, and (iii) to optimize the reactor design to overcome some barriers that impede the scaling up and transfer of the technology to practical applications. To this end, the effects of material selection, assembly parameters, flow field patterns, and operating conditions of PSE reactors on H_2O_2 electrosynthesis were systematically evaluated. The ion conduction, reaction thermodynamics, and flow field distribution in the PSE reactor were investigated using molecular dynamics (MD), density functional theory (DFT), and computational fluid dynamics (CFD) tools. Based on the obtained findings, the reactor design was optimized and a modular PSE reactor with a total electrode area of 1200 cm^2 was developed. The feasibility of the scaled-up PSE reactor for potential niche applications were then evaluated under likely operating conditions.

Results

Effects of PSE on H_2O_2 electrosynthesis

PSE microspheres packed in the middle layer of the PSE reactor play a critical role for ion conduction along their interconnected surfaces and for water flowing through their interparticle space during H_2O_2 electrosynthesis⁹. Therefore, it is expected that the properties of PSE microspheres (e.g., ion conductivity and particle size) can significantly influence H_2O_2 electrosynthesis, which however has not been well explored previously. In this study, we first compared several commercial PSEs that had been used as ion conductors for H_2O_2 electrosynthesis and other electrochemical processes (e.g., CO_2 electroreduction and electrodeionization)^{9,11,14,15}. These PSE microspheres are all made of styrene-divinylbenzene copolymer and functionalized with sulfonic acid (SA) groups, but have different ion exchange capacity and specific surface areas (see Table 1 for the characterization results). For the comparison, the various PSE microspheres with the same particle size range ($d = 300\text{--}1000\ \mu\text{m}$) were packed with a bulk density of $\sim 1100\ \text{mg}/\text{mL}$ in the middle layer of the reactor. Figure 1a shows that with increasing applied current densities, higher concentrations of H_2O_2 solutions were obtained during H_2O_2 electrosynthesis with the varying PSEs. However, for the same current density, the obtained H_2O_2 concentrations and FE decreased, while the cell voltages increased in the order of Dowex 50 W \times 8, Amberlite IR 120H, Sennate D001 \times 7, and Purolite CT-175 (Fig. 1a–c). Consequently, the energy consumption (EC) of H_2O_2 production (calculated according to Eq. 5) increased considerably from 4.83 $\text{kWh}/\text{kg}\ \text{H}_2\text{O}_2$ for Dowex 50 W \times 8 to 15.93 $\text{kWh}/\text{kg}\ \text{H}_2\text{O}_2$ for Purolite CT-175 (see SI Fig. S6).

The above results confirm that the properties of PSE microspheres can considerably influence the performance of H_2O_2 electrosynthesis. As reported in Table 1, both the ion exchange capacity and surface area of the four PSEs increase in the order of Dowex 50 W \times 8, Amberlite IR 120H, Sennate D001 \times 7, and Purolite CT-175. While the

Table 1 | Parameters of PSE microspheres tested in this study

PSE	Ion exchange capacity (meq/g)	Surface area (m^2/g)	SA group density (meq/ m^2) ^a	$R_s\ (\Omega)$ ^b
Dowex 50 W \times 8	3.1	0.025	124	1.77
Amberlite IR 120H	4.1	0.066	62.1	2.66
Sennate D001 \times 7	4.4	0.118	37.3	3.28
Purolite CT-175	4.7	23.4	0.2	8.25
Amberlyst 39WET	5.5	0.112	49.1	3.92
Amberlyst 15WET	4.5	55	0.08	7.84
Amberlyst 36WET	5.5	20.1	0.27	6.84
Lewatit K2621	5.5	31	0.18	7.51
Dowex 50 W \times 4	1.4	0.021	66.67	1.76
Purolite CT-275	5.1	24.7	0.21	2.65

^aCalculated based on the measured ion exchange capacity and surface area of PSE microspheres.

^bMeasured with a packing density of PSE microspheres of 1100 mg/mL , see SI Figs. S8 and S9 for more detail.

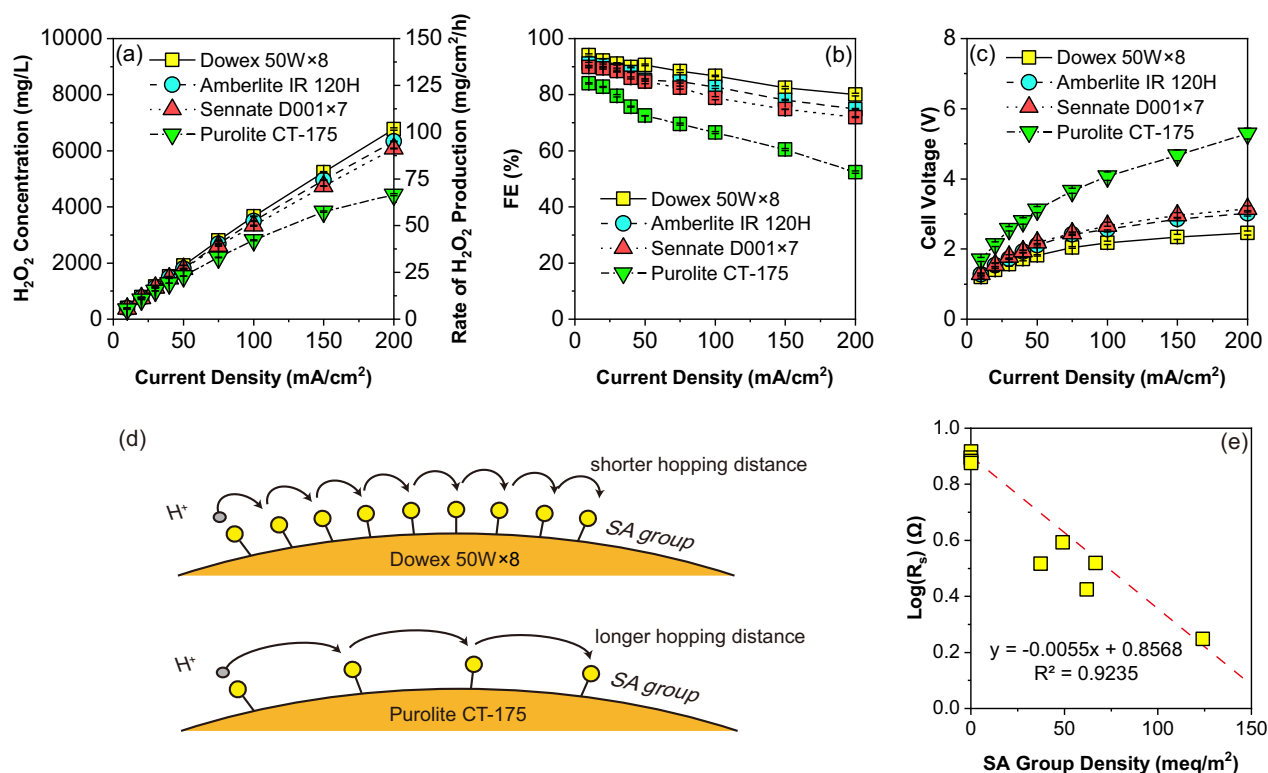


Fig. 1 | The effects of applied current densities on H₂O₂ electro-synthesis. **a** H₂O₂ concentrations and production rates, **b** Faradaic efficiency (FEs), and **c** cell voltages during H₂O₂ electro-synthesis with the PSE reactor (4 cm²) packed with various PSEs, **d** illustrations of H⁺ transfer on Dowex 50 W×8 and Purolite CT-175, and **e** the negative logarithmic relationship between the surface SA density and R_s of H⁺ conduction of ten types of PSEs (see Table 1). Operating conditions: PSE microspheres (~300–1000 μm) were packed with a packing density of ~1100 mg/mL, and

the water flow rate was fixed to 1 mL/min. The cathode and anode were fed with pure oxygen (50 mL/min) and 0.5 M H₂SO₄ (recirculated), respectively, and no AEM was used. The resistance of PSE layer used in these tests is ~0.16 Ω. All the voltages are reported without iR-correction. Each experiment was repeated at least three times. Error bars represent the standard deviation. Source data for Fig. 1a–c, e are provided as a Source Data file.

increase of ion exchange capacity means that more SA groups are available on the PSE microspheres for H⁺ conduction, the increase of surface area results in decreases in the surface density of SA groups (Table 1 and SI Fig. S7). Because H⁺ conduction on the PSE surface proceeds mainly through a hopping diffusion process between neighboring SA groups (i.e., the Grotthuss mechanism)^{16–18}, the decrease of surface density of SA groups may hamper H⁺ conduction (see Fig. 1d for the schematic illustration). To verify this inference, we measured the resistance of H⁺ conduction (R_s) of ten different types of PSE microspheres that have varied surface densities of SA groups (0.08–124 meq/m², Table 1) by an electrochemical impedance spectroscopy (EIS) method (see SI Fig. S8 for the experimental schematic). In the Nyquist plot (SI Fig. S9), the R_s of PSE was determined from the intersection of the fitting curves and Z' axis^{19,20}. As expected, R_s of the PSEs increases with decreasing their surface density of SA groups (Table 1). Moreover, a negative logarithmic relationship is found between the R_s and SA group density of the various PSEs (Fig. 1e). Similar logarithmic relationships have also been reported between the conductivity and the concentration of ion conducting composition of various solid ion conductors (e.g., crystalline polymer electrolytes and conducting glasses) and suggested to be related to the ion transfer mechanism of the conductors^{21,22}.

Corresponding to the increase of R_s, the cell voltage increased in the order of Dowex 50 W × 8, Amberlite IR 120H, Sennate D001×7, and Purolite CT-175 when the same current density was applied during H₂O₂ electro-synthesis (Fig. 1c). The increase of cell voltages in turn enhances the Joule heating effect, and thus resulted in higher reactor temperatures (see SI Fig. S10) and more significant thermal decomposition of H₂O₂. Consequently, lower concentrations of H₂O₂ were

generally obtained during electro-synthesis with PSEs that have the higher R_s (Fig. 1a and Table 1). This finding indicates that PSEs with higher surface density of SA groups (and thus H⁺ conductivity) are favorable for H₂O₂ electro-synthesis with the PSE reactor.

Figure 2 shows that by decreasing the particle size or increasing the packing density of PSE microspheres (Dowex 50 W × 8), higher concentrations of H₂O₂ solutions could be obtained during electro-synthesis (Fig. 2a, d). Meanwhile, the cell voltages decreased (Fig. 2c, f), which effectively mitigates the thermal decomposition of H₂O₂. Hence, high FEs (≥95%) of H₂O₂ production were maintained even when a high current density of 200 mA/cm² was applied during H₂O₂ electro-synthesis with the smallest and most densely packed PSE microspheres (Fig. 2b, e).

The more efficient H₂O₂ electro-synthesis with smaller and/or more densely packed PSE microspheres can be mainly attributed to the increase of contact points among the packed microspheres (see SI Fig. S11a). Due to the increase of interparticles' contact points, H⁺ can more easily transport along the interconnected surfaces of PSE microspheres, thus decreasing the R_s of H⁺ conduction and cell voltages (see SI Fig. S11b, c). However, the decrease in particle size and increase in packing density of PSE microspheres decreases the porosity of the PSE layer. Hence, higher pressures were needed to drive the DI water to pass through the PSE reactor (see SI Fig. S11e). When PSE microspheres with diameters larger than 150 μm were packed in the reactor, the water flow was very stable during H₂O₂ electro-synthesis (see SI Fig. S11e). However, when PSE microspheres with smaller diameters were packed, some microspheres could be washed away from the PSE chamber by the DI water flow, and then gradually clogged the outlet of the reactor. As a result, the water flow decreased gradually

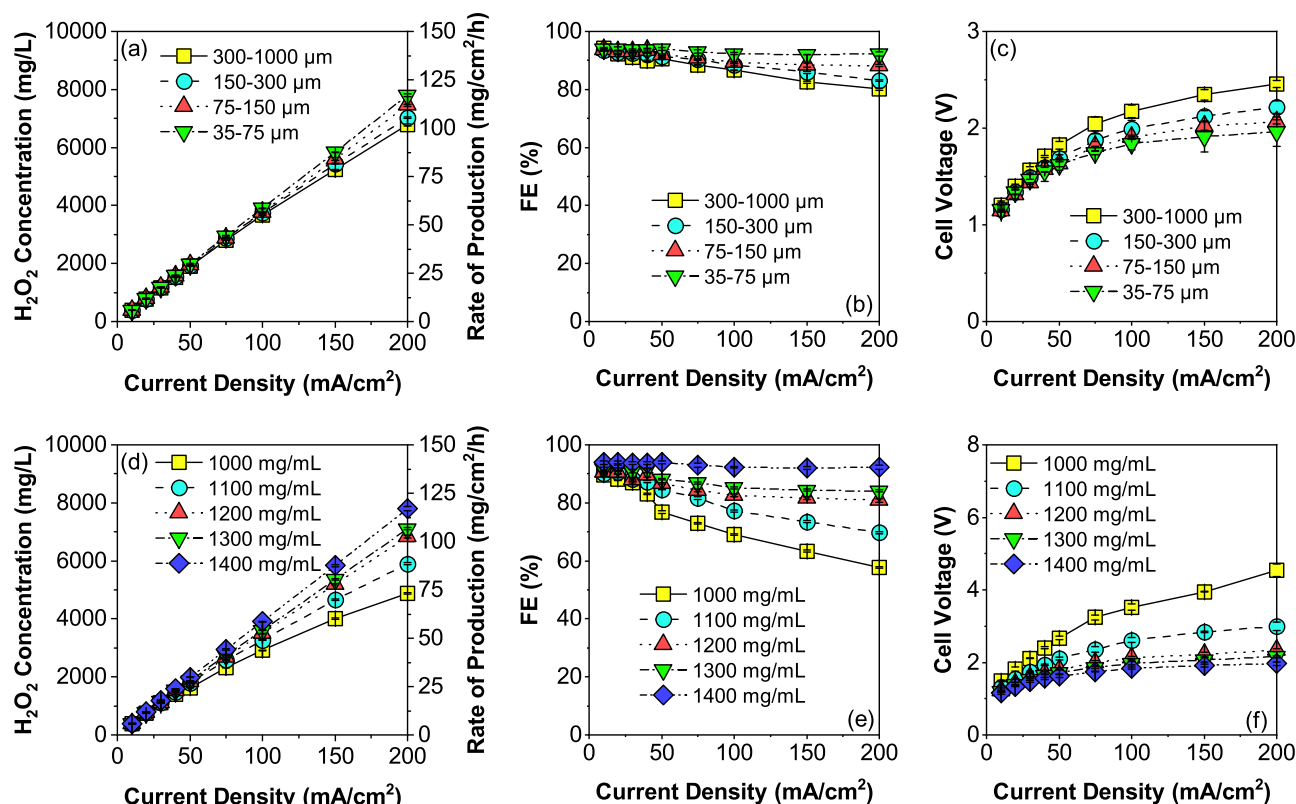


Fig. 2 | The effects of PSE diameter and packing density on H_2O_2 electro-synthesis. a, d H_2O_2 concentrations and production rates, b, e Faradaic efficiency (FEs), and c, f cell voltages during H_2O_2 electro-synthesis with the PSE reactor (4 cm^2). Operating conditions: Dowex 50 W \times 8 PSE microspheres were packed with a packing density of $\sim 1400\text{ mg/mL}$ for varying PSE diameters (Fig. 2a–c) and a diameter range of $35\text{--}75\text{ }\mu\text{m}$ for varying packing densities (Fig. 2d–f). The water flow rate was set at 1 mL/min , and the cathode and anode were fed with pure oxygen

(50 mL/min) and $0.5\text{ M H}_2\text{SO}_4$ (recirculated), respectively. The resistance of PSE layer in the reactor varied between 0.12 and $0.24\text{ }\Omega$ due to varying PSE diameters and packing densities tested in the experiments. All the voltages are reported without iR-correction. Each experiment was repeated at least three times. Error bars represent the standard deviation. Source data for Fig. 2 are provided as a Source Data file.

during H_2O_2 electro-synthesis with PSE microspheres less than $150\text{ }\mu\text{m}$ (SI Fig. S11e). These observations highlight that the particle size and packing density of PSE microspheres need to be carefully optimized to balance H^+ conduction and water flow during H_2O_2 electro-synthesis. For stable long-term operation, Dowex 50 W \times 8 microspheres with particle sizes of $150\text{--}300\text{ }\mu\text{m}$ were packed with a packing density of $\sim 1100\text{ mg/mL}$ for subsequent experiments of H_2O_2 electro-synthesis unless otherwise specified. Note that for PSE microspheres with diameters larger than $150\text{ }\mu\text{m}$, $\sim 1100\text{ mg/mL}$ was the highest packing density of PSE that could be filled in the PSE chamber ($2\text{ cm} \times 2\text{ cm} \times 2\text{ mm}$).

Effects of AEM on H_2O_2 electro-synthesis

Due to the high pressure inside the PSE reactor (Fig. S11e), water can easily intrude progressively into the internal pores of the GDE cathode if they are in direct contact. Therefore, in the absence of an AEM to separate the GDE cathode and water flow during H_2O_2 electro-synthesis, the PSE reactor failed quickly ($<12\text{ h}$) due to electrode flooding (see SI Fig. S14). This observation indicates that it is critical to use an AEM to separate the GDE cathode and water flow, while transporting HO_2^- from the cathode to the water during H_2O_2 electro-synthesis⁹. Figure 3 compares several commercial AEMs for H_2O_2 electro-synthesis with the PSE reactor. As shown, these AEMs exhibited significantly different performances, especially when high current densities ($100\text{--}200\text{ mA/cm}^2$) were applied to accelerate H_2O_2 production. In general, Sustainion XC-37T achieved the best performance in terms of the concentrations of H_2O_2 product, FEs, cell voltages, and EC, followed in order by Piperion A-40, Pention 7215-30, FAA-3-50, FAA-3-PK-130, and

AMI-7001 (Fig. 3a–c and SI Fig. S15). This trend can be mainly attributed to the different conductivity of the AEMs. As shown in Fig. 3d, the R_s of HO_2^- conduction of the six AEMs increased in the order of Sustainion XC-37T, Piperion A-40, Pention 7215-30, FAA-3-50, FAA-3-PK-130, and AMI-7001 (see SI Fig. S16 for the Nyquist plots of the AEMs). Therefore, for the same applied current density, the cell voltage during H_2O_2 electro-synthesis will increase in the same order for the six AEMs, as shown in Fig. 3c.

DFT calculations and MD simulation suggest that the different HO_2^- conductivity of the AEMs can be possibly explained by the differing hydrophilicity of neighboring groups around the quaternary ammonium (QA) in their molecular structure. Although all the AEMs are all functionalized with QA for HO_2^- conduction, their polymer backbones are different (see SI Fig. S17 and Supplementary Data 1 for the structure details, note that the molecular structure of FAA-3-50 and FAA-3-PK-130 is not openly available yet). For example, the QA group in Sustainion XC-37T is in an imidazole moiety and bridged by a methylene to a benzene ring, whereas the QA in AMI-7001 is directly connected to a benzene ring and three methyl groups. DFT calculations indicate that the neighboring benzene ring of the QA group in AMI-7001 is substantially more hydrophobic than the neighboring groups of QA in Sustainion XC-37T, Piperion A-40, and Pention 7215-30 (see SI Fig. S17 for more detail). As a result, more water molecules will be pushed toward the QA group of AMI-7001, which in turn causes stronger hydrophilic attraction between the QA group and HO_2^- and thus hamper HO_2^- conduction (see Fig. 3e for the illustration). Consistently, the MD simulation shows that the coordination number of water molecules around QA of AMI-7001 is higher than that of the

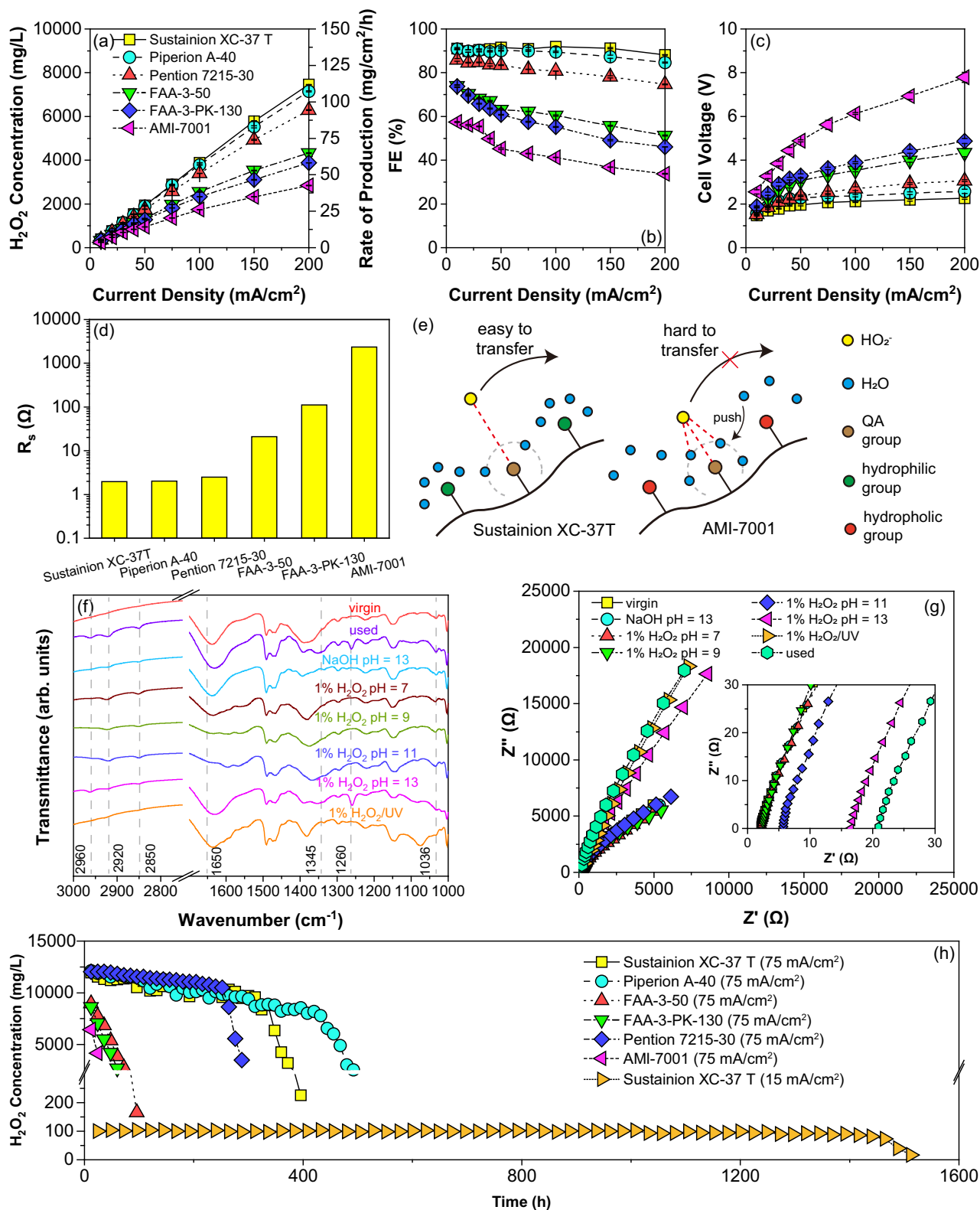


Fig. 3 | The effects of AEMs on H_2O_2 production. **a** H_2O_2 concentrations and production rates, **b** Faradaic efficiency (FEs), **c** cell voltages as a function of applied current density during H_2O_2 electro-synthesis with the PSE reactor (4 cm^2) with varying AEMs, **d** resistance of HO_2^- conduction of AEMs, **e** illustration of HO_2^- transfer in Sustaining XC-37T and AMI-7001, **f** ATR-IR spectra and **g** Nyquist plots of the virgin Sustaining XC-37T AEM and those used for H_2O_2 electro-synthesis or treated by different processes (the inset shows the zoomed-on area from 0 to 30 Ω), **h** stability of PSE reactors during H_2O_2 electro-synthesis with various AEMs at

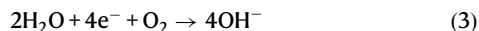
15–75 mA/cm^2 . The operating conditions were the same as described in Fig. 2, with the exception that during the stability experiment at 15 mA/cm^2 , a reverse osmosis filtrate of tap water was used to replace DI water as the feeding water to the PSE reactor. The resistance of PSE layer in the reactor is $\sim 0.16\ \Omega$. All the voltages are reported without iR-correction. Each experiment was repeated at least three times except for stability test. Error bars represent the standard deviation. Source data for Fig. 3a–d, f–h are provided as a Source Data file.

other three AEMs (see SI Fig. S18g and Supplementary Data 2–9 for the configurations). Meanwhile, the MD simulated HO_2^- conductivity of AMI-7001 (0.85 mS/cm) is considerably lower than that of Sustainion XC-37T, Piperion A-40, and Pention 7215-30 (5.29, 3.86, and 1.58 mS/cm, respectively, see SI Fig. S19 for more information). Overall, the simulation results are in line with the EIS measurement (Fig. 3d) and suggest that AEMs with low hydrophobic polymer backbones are beneficial for HO_2^- conduction. This information may provide useful guide for the development of AEMs for HO_2^- conduction.

Figure 3h shows that H_2O_2 concentrations declined at significantly different rates during long-term H_2O_2 electrosynthesis experiments with the varying AEMs. For FAA-3-50, FAA-3-PK-130, and AMI-7001, the produced H_2O_2 concentrations decreased rapidly from initially ~7000–9000 mg/L to negligible levels after only ~48–96 h operation. In comparison, H_2O_2 concentrations decreased only gradually during the first 250–450 h with Pention 7215-30, Sustainion XC-37T, and Piperion A-40, but then also dropped abruptly afterwards.

EIS and linear sweep voltammetry (LSV) analysis indicated that there are no significant changes in the ion conductivity of the PSE microspheres and in the ORR activity of the GDE cathode before and after the long-term experiments (SI Fig. S20). In contrast, significant changes were observed for the morphology of the AEMs (see SI Fig. S21). With increasing the experimental duration, the originally smooth surface of Sustainion XC-37T AEM became rugged and fibrous (SI Figs. S21a, b), and evident breakages and disintegration were observed for the AEM when the long-term experiment was terminated due to the reactor failure (~500 h, SI Fig. S21c). These observations indicate that the polymer structure of AEMs is substantially degraded during H_2O_2 electrosynthesis, thus leading to the declined performance and reactor failure.

Notably, the lifetime of the AEMs observed herein is considerably shorter than that observed during alkaline water electrolysis and CO_2 electro-reduction^{23,24}. For example, it has been shown that the Sustainion XC-37T AEM could maintain a stable operation for 2000 h during alkaline water electrolysis at even a considerably higher current density of 1000 mA/cm²²³. During alkaline water electrolysis, AEMs are exposed to high concentrations of OH^- (e.g., pH = 14) formed from hydrogen evolution reaction (Eq. 3). In contrast, AEMs are exposed to lower concentrations of OH^- , but high concentrations of $\text{H}_2\text{O}_2/\text{HO}_2^-$ ($\text{pK}_a(\text{H}_2\text{O}_2) = 11.6$, Eq. 2) during H_2O_2 electrosynthesis (Eq. 1). This comparison suggests that $\text{H}_2\text{O}_2/\text{HO}_2^-$ is possibly the main species that accelerated the degradation of AEMs during H_2O_2 electrosynthesis. In addition, some studies have hypothesized that hydroxyl radicals ($\cdot\text{OH}$) formed during H_2O_2 electrosynthesis are possibly the main species for AEM degradation¹¹.



To reveal the mechanism of AEM degradation, the structure of the virgin and used Sustainion XC-37T AEM, as well as AEMs that had been soaked in NaOH (pH = 13) and H_2O_2 solutions (1%) with varying pH levels (pH = 7–13) for 120 h, or treated by ultraviolet/ H_2O_2 (1%, pH = 7) process (120 h) was examined using attenuated total reflection infrared spectroscopy (ATR-IR) (Fig. 3f). Compared with the virgin AEM, the intensity of 1036 and 1260 cm⁻¹ band (stretching vibration of C–N, see SI Table S2 for more information) of the used AEM increased. This change can be probably attributed to the transformation of C=N in the imidazole group to C–N^{25,26}. Note that the C=N stretching band (~1630–1650 cm⁻¹²⁷) overlaps the strong vibration band of –OH (bending vibration at ~1630–1640 cm⁻¹^{28,29}) and thus cannot be distinguished in the spectra. In addition, several new bands emerge for the used AEM, including 1345 cm⁻¹ (–COO– asymmetric vibration), 2960 cm⁻¹ (–COOH bending vibration), and 2850 and 2920 cm⁻¹ (–CH₃ asymmetric stretch)^{30–32}. These observations confirm that the polymer

structure of Sustainion XC-37T AEM has been substantially changed during H_2O_2 electrosynthesis.

Interestingly, while the IR spectra of AEMs soaked in NaOH (pH = 13) and H_2O_2 solutions with pHs lower than the pK_a of H_2O_2 (11.6) exhibit no significant changes as compared to that of the virgin AEM, the IR spectra of AEM soaked in H_2O_2 solutions at pH 13 exhibits similar changes as have been observed for the used AEM, e.g., the increase of 1036 cm⁻¹ band and the emergence of 1260, 1345, and 2960 cm⁻¹ bands. These comparisons indicate that OH^- and H_2O_2 are not very reactive with AEMs, whereas HO_2^- (which is the predominant species of $\text{H}_2\text{O}_2/\text{HO}_2^-$ at pH higher than the pK_a of H_2O_2) is probably the main species that causes AEM degradation during H_2O_2 electrosynthesis. Consistently, DFT calculations show that due to the strong nucleophilicity of HO_2^- , it can attack the QA groups of AEMs and thus cause AEM degradation (see SI Figs. S22–S24 and Table S3–S4 for more detail). Corresponding to its significant structural changes, the ion conductivity of the AEM soaked in H_2O_2 solutions at pH 13 decreased substantially, as has been shown for the used AEM (Fig. 3g). In comparison, the ion conductivity of AEMs soaked in other solutions exhibit insignificant or only small decreases (H_2O_2 solution at pH 11) as compared to that of the virgin AEM. These observations corroborate that HO_2^- is the main species responsible for AEM degradation during H_2O_2 electrosynthesis.

It should be noted that although the UV/ H_2O_2 treatment also changed the IR spectra and morphology of Sustainion XC-37T AEM as compared to that of the virgin AEM (Fig. 3f and SI Fig. S21i), the changes (e.g., the emergence of 1074 cm⁻¹ band due to asymmetry vibration of C–OH) are significantly different from those observed for the AEM used for H_2O_2 electrosynthesis³³. This observation suggests that $\cdot\text{OH}$ is possibly not the main reactive species that causes AEM degradation during H_2O_2 electrosynthesis as previously assumed.

Overall, the results shown above indicate that while an AEM is critical to avoid electrode flooding and transport HO_2^- during H_2O_2 electrosynthesis with the PSE reactor, the low stability of QA functionalized AEM in the presence of HO_2^- can severely limit the reactor to achieve the desired lifetime. With decreasing the concentrations of produced H_2O_2 solutions (~100 mg/L) by using smaller current densities (15 mA/cm²) during H_2O_2 electrosynthesis, the lifetime of Sustainion XC-37T AEM could be extended to ~1500 h (Fig. 3h). However, this duration is still insufficient for many industrial applications. Therefore, more stable AEMs need to be developed for H_2O_2 electrosynthesis with the PSE reactor. In addition, Rawah et al. proposed to replace the AEM with a PTFE layer to improve the stability of the PSE reactor for H_2O_2 electrosynthesis¹¹. However, the PSE reactor with the PTFE layer was tested for only 50 h at a current density of 70 mA/cm². Further studies are still required to verify the long-term stability of the PSE reactor with the PTFE layer.

Effects of feeding materials on H_2O_2 electrosynthesis

Besides producing pure H_2O_2 solutions with DI water, it is of great interest if the PSE reactor can offer a possible way to produce H_2O_2 with more readily available low-conductivity water, e.g., tap water and fresh water. This will be more convenient and economical for many applications, for example, decentralized water treatment and textile bleaching, where DI water may not be easily available and/or pure H_2O_2 solutions are not necessarily needed. To test the feasibility of the PSE reactor for producing H_2O_2 in low-conductivity water matrix, we changed the DI water flow to a tap water flow (conductivity = 748 μS/cm, see SI Table S5 for other water quality parameters) during H_2O_2 electrosynthesis. However, the results show that the PSE reactor failed to produce H_2O_2 after only 10 h operation with the tap water, in contrast to the stable H_2O_2 production with DI water (Fig. 4a). Meanwhile, water constituent analysis shows that the concentrations of divalent ions (e.g., Ca^{2+} , Mg^{2+} , and SO_4^{2-}) in the tap water decreased evidently after it flowed through

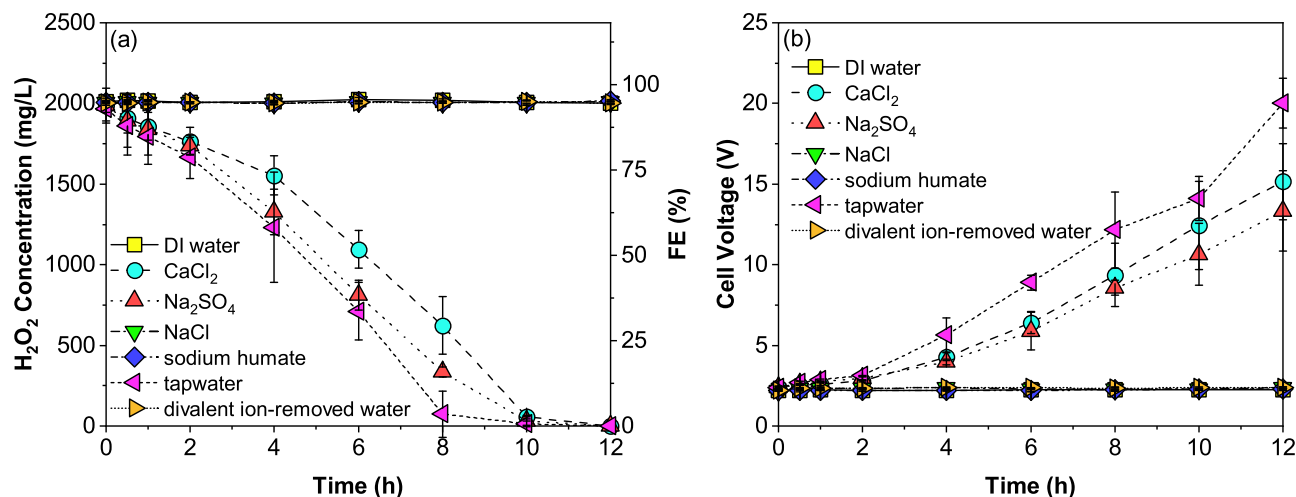


Fig. 4 | Effects of water matrices on H_2O_2 electrosynthesis. **a** H_2O_2 concentrations and Faradaic efficiency (FEs), **b** cell voltages during H_2O_2 electrosynthesis with the PSE reactor (4 cm^2). The operating conditions were the same as described in Fig. 2. The resistance of PSE layer in the reactor is $\sim 0.16\ \Omega$. All the voltages are

reported without iR-correction. Each experiment was repeated at least three times. Error bars represent the standard deviation. Source data for Fig. 4 are provided as a Source Data file.

the PSE reactor, while the concentrations of other constituents such as monovalent ions (e.g., Na^+ and Cl^-) and dissolved organic matter (DOM, measured as total organic carbon) remained almost unchanged (see SI Table S5). Therefore, we speculated that the reactor failure is possibly caused by the divalent ions in the tap water. Due to the strong electrostatic attraction between divalent cations/anions and SA/QA groups, divalent cations (e.g., Ca^{2+} and Mg^{2+}) may be stably adsorbed on SA sites of PSE microspheres and PEM, while anions (e.g., SO_4^{2-}) may be strongly adsorbed on QA sites of the AEM. This may interrupt the hopping diffusion of H^+ through the PSE microsphere layer and PEM, as well as the hopping of HO_2^- through the AEM, thus causing the failure of the PSE reactor for H_2O_2 production.

To verify this inference, we prepared several solutions by adding varying concentrations of CaCl_2 , Na_2SO_4 , NaCl , or sodium humate in deionized water, and then fed the various solutions through the PSE reactor for H_2O_2 electrosynthesis. As expected, the performance of H_2O_2 production deteriorated quickly when the reactor was fed with CaCl_2 and Na_2SO_4 solutions, but maintained stably when fed with NaCl and sodium humate solutions. Furthermore, we found that by pre-treating the tap water with ion exchange to remove the divalent ions (e.g., Ca^{2+} , Mg^{2+} , and SO_4^{2-}), the PSE reactor maintained stable H_2O_2 production as had been fed with the DI water (Fig. 4a). These results confirm that divalent ions are the major water constituents that caused the reactor failure, whereas monovalent ions and DOM (when present at similar concentrations of the tap water) will not significantly influence H_2O_2 electrosynthesis with the PSE reactor (see SI Fig. S25 for more information). This finding suggests that the PSE reactor may provide a convenient and economical way to produce H_2O_2 in some niche applications, such as potable water reuse, where UV/ H_2O_2 is often used to degrade residual chemical pollutants (e.g., N-nitrosodimethylamine and 1,4-dioxane) in reverse osmosis (RO) filtrate³⁴. In such scenarios, because the divalent ions have been effectively removed by RO filtration, the filtrate can be directly fed into the PSE reactor to produce H_2O_2 for the following UV/ H_2O_2 treatment. Indeed, Fig. 3h shows that the PSE reactor maintained stable H_2O_2 production for $\sim 1400\text{ h}$ until the reactor failed due to AEM degradation when it was fed with an RO filtrate of the tap water.

Currently, the PSE reactor needs to use pumps to supply oxygen/air to the GDE cathode and to recirculate H_2SO_4 solutions in the anode compartment to improve the ionic conductivity on the anode side^{9,11}. However, the use of pumps and H_2SO_4 solutions is undesired (and possibly impractical) in some applications, such as point-of-use water

treatment at household levels³⁵. To avoid the use of pumps and H_2SO_4 , we modified the PSE reactor to expose the gas diffusion layer of the GDE directly to ambient air, so that oxygen in the air can diffuse naturally to the catalyst layer for H_2O_2 electrosynthesis (see SI Fig. S4 for the modified PSE reactor). Figure 5a shows that within the current density range of $10\text{--}200\text{ mA/cm}^2$, the concentrations and production rates of H_2O_2 were generally similar or only slightly lower during H_2O_2 electrosynthesis with natural air diffusion than with the pumped O_2/air flow. This finding indicates that sufficient oxygen can be supplied by natural air diffusion for H_2O_2 electrosynthesis with the PSE reactor³⁶.

In addition, we changed the catalyst-coated substrate (CCS) anode configuration used in current PSE reactors to the catalyst-coated membrane (CCM) configuration by directly hot-pressing a mixture of IrO_2 catalysts and Nafion ionomer onto the PEM. It is expected that because of its strong intrinsic acidity, Nafion ionomer can effectively conduct H^+ at the anode during H_2O_2 electrosynthesis. As shown in Fig. 5d and SI Fig. S26, there is insignificant difference in H_2O_2 production when DI water or H_2SO_4 solutions (0.5 M) was fed in the anode compartment. Furthermore, we found that because ample water can permeate from the middle PSE layer through the PEM to the anode side by concentration diffusion and hydraulic penetration (see SI Fig. S27 for more information), the PSE reactor can stably produce H_2O_2 at high current densities (up to 680 mA/cm^2) even without using a pump to feed DI water in the anode compartment. Overall, these modifications avoid the use of pumps and H_2SO_4 , and thus considerably simplify the PSE reactor configurations and facilitate its operation in practical applications.

Notably, the performance of the PSE reactor is considerably better than those reported for electrochemical reactors using salt-based liquid electrolytes (Table 2)⁸. In addition, the H_2O_2 produced by PSE reactor contains no salts and can therefore be directly used for many applications.

Scaling up the PSE reactor for H_2O_2 electrosynthesis

To test the scalability of the PSE reactor, we first designed an enlarged PSE reactor with 25 cm^2 electrodes based on the optimized parameters determined for the small PSE reactor (4 cm^2). Figure 6a–c shows that for the same applied current density, the rates and FEs of H_2O_2 production decreased substantially for the larger PSE reactor, while the cell voltage increased considerably. Similar deteriorations of H_2O_2 electrosynthesis performance during reactor scaling up were also

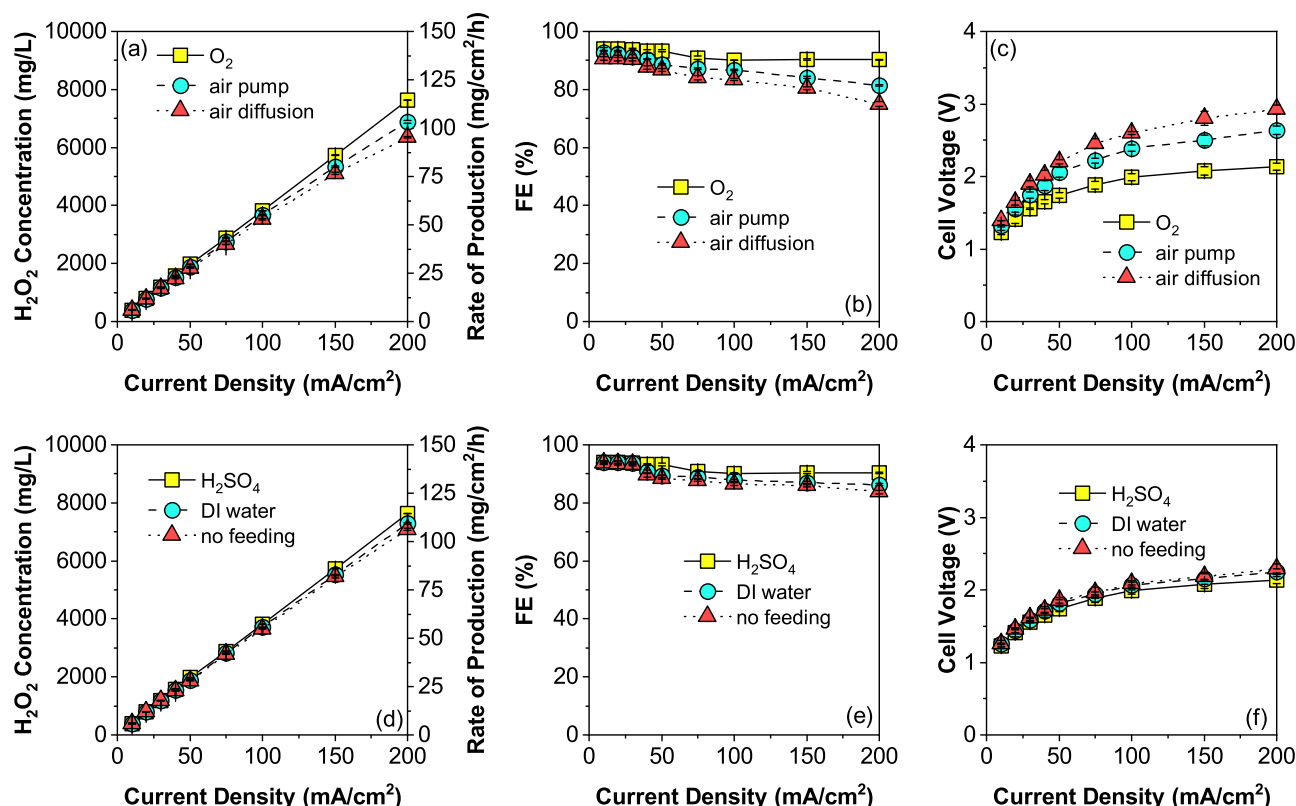


Fig. 5 | The influence of cathodic feeding and anodic feeding on H_2O_2 electro-synthesis. a, d H_2O_2 concentrations and production rates, b, e Faradaic efficiency (FEs), c, f cell voltages. The operating conditions were the same as described in Fig. 2, except for the changes of cathode and anode feeding materials. The

resistance of PSE layer in the reactor is -0.16Ω . All the voltages are reported without iR-correction. Each experiment was repeated at least three times. Error bars represent the standard deviation. Source data for Fig. 5 are provided as a Source Data file.

observed in the previous study⁹. To reveal the reasons for the declined performance, we simulated the flow field in the PSE microsphere layer using CFD tools. The results show that with increasing the electrode size, the flow field in the PSE microsphere layer became increasingly uneven. As shown in Fig. 6d, the fluid velocity decreases quickly from the inlet of the enlarged reactor, resulting in a significant fraction of dead zones in the PSE microsphere layer. Since the H^+ transfer resistance of PSE is negatively related to the flow rate, these dead zones will cause an uneven current and potential distribution on the electrode surface, and thus decrease current efficiencies and increase electrode overpotentials during electrolysis^{37,38}. Moreover, due to the slow flow velocity in the dead zones, the mass transfer process in the reactor is considerably impeded, which may promote side reactions. For example, when H_2O_2 produced in the dead zones cannot be effectively carried by the water flow out of the reactor, the thermal decomposition of H_2O_2 will be considerably enhanced.

To improve the flow pattern in the enlarged reactor, we designed a serpentine flow field plate and filled the PSE microspheres in the channels. As shown in Fig. 6d, the serpentine flow channel considerably improves the uniformity of flow field. As a result, the rates and FEs of H_2O_2 production increased substantially, while the cell voltages decreased considerably (Fig. 6a–c). These observations indicate that the PSE reactor can be successfully scaled up based on the optimized parameters determined with the small reactor (4 cm^2) and highlight the importance of optimizing the flow field when scaling up the PSE reactor.

Based on this finding, we further extended the electrode area to 100 cm^2 and designed a 12-unit modular electrode stack with a total electrode area of 1200 cm^2 for H_2O_2 electro-synthesis (see SI Fig. S28 and Supplementary Movies 1 and 2 for the assembly and operation of the stack reactor). Compared with the previously reported largest PSE reactor (80 cm^2)⁹, the electrode area of the stack reactor was increased

by 15 times, and the performance of H_2O_2 electro-synthesis was substantially improved. For example, with an applied current density of 100 mA/cm^2 , $\sim 17,000 \text{ mg/L}$ H_2O_2 solutions could be produced with a cell voltage of 4.2 V , a total rate of production of $\sim 60.9 \text{ g/h}$ (on a 100 wt % basis), and a FE of 80% by the stack reactor (see Fig. 6e and SI Fig. S30a). In comparison, the cell voltage reached about 4.8 V , and the rate and FE of H_2O_2 production were only $\sim 3.2 \text{ g/h}$ and $\sim 63\%$ during H_2O_2 electro-synthesis with the previous PSE reactor under similar operation conditions (100 mA/cm^2 , $\sim 18,000 \text{ mg/L}$ H_2O_2)⁹. According to the FE and cell voltages observed during the experiments, the energy consumption of H_2O_2 electro-synthesis with the stack reactor is calculated to be $3.67\text{--}12.74 \text{ kWh/kg}$ H_2O_2 (on 100 wt% basis) using Eq. 5 (see SI Fig. S30 for more information). Based on the electricity cost of 0.066 USD/kWh ⁸, the energy cost corresponds to $\sim 0.24\text{--}0.84 \text{ USD/kg}$ H_2O_2 , which is much lower than the sales price of H_2O_2 solutions, e.g., $0.7\text{--}1.2$ and $6.8\text{--}10.3 \text{ USD/kg}$ on 100 wt% basis for industrial and food grade H_2O_2 , respectively.

Under the tested conditions (200 mA/cm^2), $\sim 2.5 \text{ kg}$ of pure H_2O_2 can be produced with the 12-unit modular PSE reactor each day. This quantity is sufficient to treat $\sim 833\text{--}5000 \text{ m}^3/\text{d}$ water in potable water reuse and drinking water treatment based on typical H_2O_2 doses applied in these applications ($\sim 0.5\text{--}3 \text{ mg/L}$)^{35,39}. By adding more electrode stacks, higher H_2O_2 production capacity could be achieved for large-scale applications.

To evaluate the long-term stability of the scaled-up reactor, it was continuously operated for 480 h under current densities of 25 and 50 mA/cm^2 . Figure 6f shows that H_2O_2 production was generally stable during the first 408 h, but then decreased gradually. This trend is similar to what has been observed for the small reactor (Fig. 3h) and can be mainly attributed to the gradual degradation of AEM during H_2O_2 electro-synthesis. Overall, the results presented herein indicate that by

Table 2 | Comparison of electrochemical reactors for H₂O₂ electrosynthesis

Electrolyte	j (mA/cm ²)	Cell voltage (V)	H ₂ O ₂ conc. (mg/L)	FE (%)	EC (kWh/kg H ₂ O ₂)	Ref.
PSE	10	1.48 (1.47 ^a)	385	91.0	2.56 (2.54 ^a)	This study
	20	1.70 (1.67 ^a)	760	90.0	2.98 (2.93 ^a)	
	50	1.95 (1.88 ^a)	1903	91.5	3.36 (3.25 ^a)	
	100	2.11 (1.98 ^a)	3781	91.9	3.62 (3.39 ^a)	
	200	2.26 (1.99 ^a)	7147	88.1	4.05 (3.57 ^a)	
PSE	12	−(1.69 ^a)	860	91.5	−(2.91 ^a)	9
	23	−(1.80 ^a)	1730	92.1	−(3.08 ^a)	
	53	−(1.93 ^a)	4530	96.4	−(3.16 ^a)	
	108	−(2.04 ^a)	8780	93.4	−(3.44 ^a)	
	200	−(2.13 ^a)	16,300	86.7	−(3.87 ^a)	
PSE	13	1.69 (1.50 ^b)	—	93.9	2.84 (2.52 ^b)	52
	57	2.73 (1.86 ^b)	—	93.9	4.58 (3.12 ^b)	
	126	4.15 (2.31 ^b)	—	93.5	7.00 (3.90 ^b)	
	183	5.29 (2.62 ^b)	—	92.4	9.03 (4.47 ^b)	
	258	6.58 (2.83 ^b)	—	89.7	11.57 (4.98 ^b)	
PSE	50	2.16	—	—	—	53
	100	2.45	—	—	—	
	150	2.57	—	85.0	4.55	
	200	2.70	—	—	—	
0.1 M Na ₂ SO ₄	22.2	2.75	10,000	78.8	5.50	54
0.05 M Na ₂ SO ₄	20	2.49	—	87.2	4.50	36
	80	4.69	—	76.9	9.61	
	120	5.82	—	71.2	12.89	
	200	7.83	—	65.7	18.78	
	240	8.14	—	66.6	19.28	
0.05–0.1 M Na ₂ SO ₄	10	3.03	10	90.8	5.26	55
	20	3.90	19	88.2	6.97	
	40	5.45	39	92.5	9.29	
	75	7.40	70	88.7	13.16	
	100	9.78	91	86.3	17.88	
0.05–1 M Na ₂ SO ₄	50	2.21	11,995	75.6	4.61	8
	100	2.53	21,281	67.1	5.95	
	150	3.14	28,662	60.2	8.23	
	200	3.68	34,138	53.8	10.79	

^aWith 70% iR compensation.^bWith 80% iR compensation.

carefully optimizing the reactor design and operational parameters, the PSE reactor can be successfully scaled up to economically produce H₂O₂ for large practical applications, e.g., disinfection (see SI Fig. S31 for more information). Nevertheless, more durable AEMs need to be developed to improve the lifetime of PSE reactors for long-term operations.

Discussion

This study systematically investigated and optimized the design of PSE reactors for H₂O₂ electrosynthesis. The results indicate that PSEs with high surface sulfonate group densities and AEMs

with hydrophilic polymer backbone are favorable for H⁺ and HO₂[−] conduction, and thus allow efficient H₂O₂ electrosynthesis. The employment of natural air diffusion cathodes and catalyst-coating membrane anodes enables the PSE reactor to produce H₂O₂ without the need to use gas pumps to supply oxygen/air and using sulfuric acid as the anolyte, which considerably simplifies the configuration of PSE reactors and facilitates their operation. By designing serpentine channels to improve the flow pattern in the PSE layer, the PSE reactor could be successfully scaled up without considerable decline in H₂O₂ electrosynthesis performance. Under industrially relevant current densities (100–200 mA/cm²), the scaled-up PSE reactor (1200 cm² electrode) could produce up to ~2.5 kg pure H₂O₂ (~83 kg of 3% aqueous H₂O₂ solutions), which is sufficient for some small applications, such as decentralized water treatment and disinfection. Compared with the sales prices of H₂O₂ stocks, the energy costs of H₂O₂ electrosynthesis with PSE reactors are significantly lower (0.2–0.8 USD/kg H₂O₂). Moreover, the produced H₂O₂ solutions contain no salts and can be directly used in various applications. These results demonstrate that the PSE reactors can provide an economically competitive and attractive way to produce H₂O₂ for some practical applications.

During H₂O₂ electrosynthesis, HO₂[−] can attack the QA groups of AEMs through the nucleophilic reaction, and thus cause the gradual degradation of AEMs. Therefore, while AEMs are indispensable to avoid electrode flooding and transport HO₂[−] during H₂O₂ electrosynthesis, their low stability in the presence of high concentrations of HO₂[−] is the main bottleneck of the PSE reactors for long-term stable operation. Further studies are needed to develop more durable AEMs to improve the lifetime of PSE reactors for H₂O₂ electrosynthesis.

Methods

Materials

Sulfuric acid (H₂SO₄) and hydrochloric acid (HCl) were purchased from Beijing Chemical Works (China). Calcium chloride (CaCl₂) and sodium hydroxide (NaOH) were purchased from Xilong Scientific Co., Ltd. (China). Sodium chloride (NaCl) and sodium humate were purchased from Macklin Co., Ltd. (China). Agar and LB Broth were purchased from Aladdin Co., Ltd. (USA). All the chemicals were of AR grade and used without further purification. XC-72R carbon black powder was purchased from Sinero Co., Ltd. (China). HCPI35 carbon paper was purchased from Hesen Co., Ltd. (China). Before experiments, the porous solid electrolytes (PSEs) and anion exchange membranes (AEMs) were thoroughly washed with DI water produced by a Master Touch-Q water purifier (Hetai Co., Ltd., China), and then kept in DI water prior to use. The proton exchange membrane (PEM) with an IrO₂ coating amount of ~3 mg/cm² and electrochemical cells were provided by CAS Cotrun Co., Ltd. (China) and Chuxi Industrial Co., Ltd. (China), respectively.

Preparation of GDEs

GDEs were prepared using a modified CCS strategy of membrane electrode assembly. Briefly, 10 mg of XC-72R carbon black (Cabot Co., Ltd., USA) powder and 50 μL of AEM ionomer were sequentially dispersed into 1 mL of 75% alcohol (AR) under ultrasonication in an ice bath. After 10 min of ultrasonication, the as-prepared ink was sprayed onto a 3.3 cm × 3.3 cm HCPI35 carbon paper (Hesen Co., Ltd., China) by an airbrush (catalyst loading: ~1 mg/cm²). Later, the carbon paper was dried naturally. Note that during H₂O₂ electrosynthesis with PSE reactors, the local pH at the cathode is highly basic because of the consumption of H⁺ in the 2e-ORR reaction¹¹. Because carbon materials are highly active and selective for 2e-ORR under alkaline conditions (SI Fig. S5)^{6,9}, the XC-72R carbon black powder was directly used as the catalyst for H₂O₂ electrosynthesis without further tailoring (e.g., oxygen-, nitro-doping, or transition metal decoration^{40–42}) in the present study.

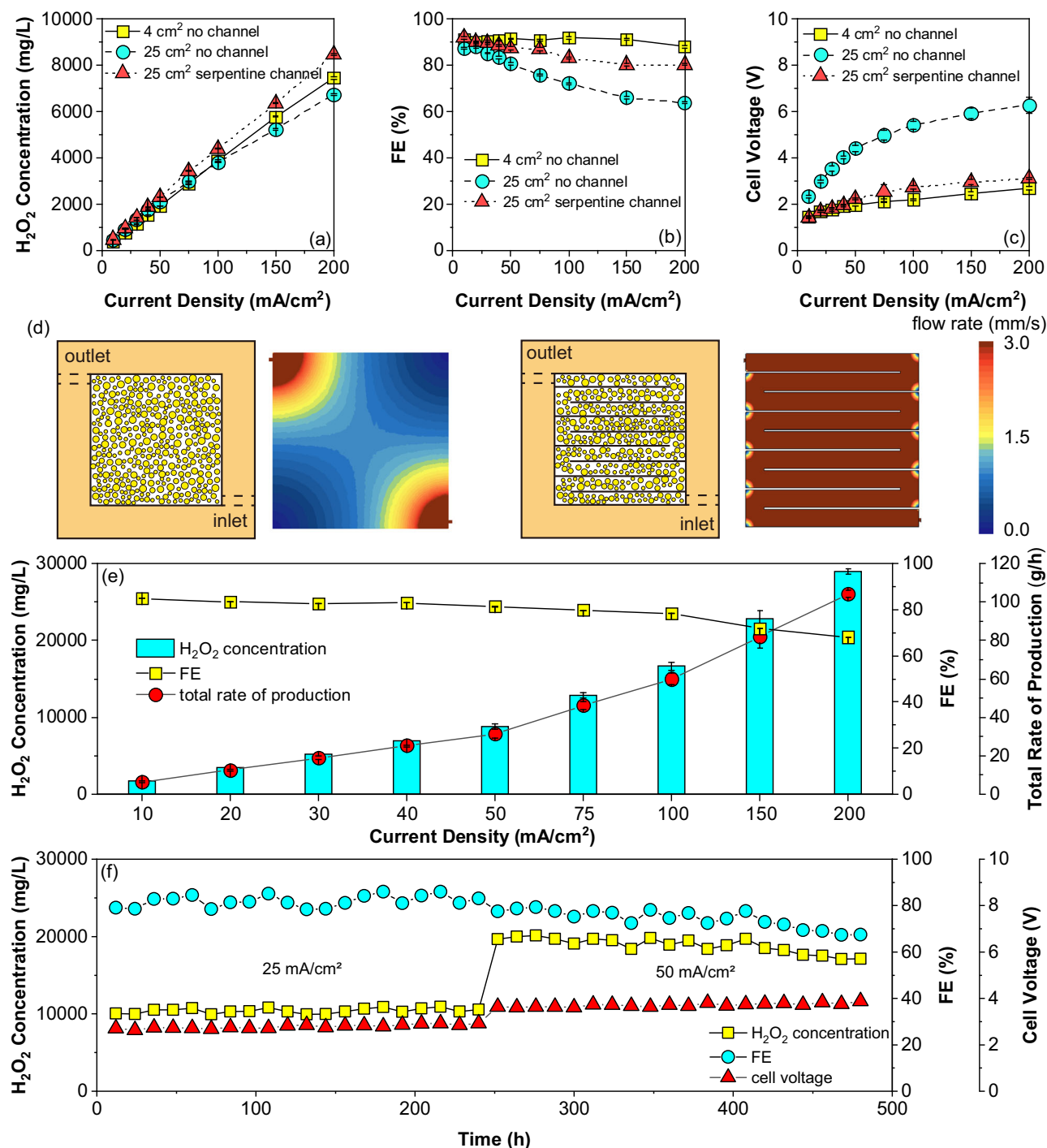


Fig. 6 | The influence of reactor scaling-up on H_2O_2 electrosynthesis. **a** H_2O_2 concentrations, **b** Faradaic efficiency (FEs), and **c** cell voltages; **d** illustration and computed flow rate of 25 cm^2 reactor without and with a serpentine channel, **e** H_2O_2 concentration, FE, and total rate of production of the 1200 cm^2 PSE reactor with varying current densities, and **f** stability of the 1200 cm^2 PSE reactors during H_2O_2 electrosynthesis with 25 mA/cm^2 (0–240 h) and 50 mA/cm^2 (240–480 h) at an ambient temperature of -10°C . The DI water flow rate was 1, 5, and 60 mL/min for

the 4, 25, and 1200 cm^2 reactors, respectively (Fig. 6a–e), and was 25 mL/min for the stability experiments with the 1200 cm^2 reactor. The resistance of PSE layer is $-0.16\ \Omega$ for the 4 cm^2 reactor, $-0.03\ \Omega$ for the 25 cm^2 reactor, and $-0.01\ \Omega$ for the 1200 cm^2 reactor, respectively. All the voltages are reported without iR-correction. Each experiment was repeated at least three times except for stability test. Error bars represent the standard deviation. Source data for Fig. 6a–c, e–f are provided as a Source Data file.

Electrochemical H_2O_2 production

The assembling method of PSE reactor is shown in SI Fig. S1a. The effective area of both anode (IrO_2 coated Nafion N115 CCM) and cathode (GDE) was 4 cm^2 ($2\ \text{cm} \times 2\ \text{cm}$). A titanium felt was used as the anode gas diffusion layer. To transport water and oxygen to the electrodes, two serpentine flow channels (2 mm width and 2.5 mm depth) were carved on two titanium endplates, respectively. The chamber placed between

the PEM and AEM was packed with PSE microspheres (thickness of 2 mm). The principle and operating schematic of PSE cell are shown in SI Fig. S1b, c. The PSEs were purchased and kept in bags, and AEMs were purchased and stored in DI water prior to use. In some experiments, a thermocouple or pressure meter was inserted into the PSE chamber to measure the temperature and internal pressure of the flow cell (see SI Figs. S2 and S3). To evaluate the scalability of the PSE reactor, two

enlarged reactors with 25 cm² (5 cm × 5 cm) of electrode and 1200 cm² of electrode stack (10 cm × 10 cm, 12 pairs) were manufactured using a similar cell structure (see SI Fig. S28 for more detailed description).

During H₂O₂ electrosynthesis, an oxygen gas (50 mL/min) and freshly prepared 0.5 M H₂SO₄ solution (pH = −0 ± 0.3) were fed through the cathode and anode compartment, respectively, while DI water (pH = −7 ± 0.3) was passed through the PSE chamber (see SI Fig. S1c). The backpressure of the GDE compartment was monitored using a gas pressure meter (see SI Fig. S3). The flow rate of DI water was adjusted to preset values by varying the pressure of the peristaltic pump. All experiments were conducted at least twice (with the exception of long-term stability tests), and the standard deviations are shown as error bars in the figures.

In some experiments, the thickness of the PSE chamber was increased to 5 mm, which allowed a thermocouple or pressure meter to be inserted into the PSE layer to measure the temperature and internal pressure of the flow cell (see Figs. S2 and S3). In addition, to avoid the use of pumps and H₂SO₄, the PSE reactor was modified to expose the gas diffusion layer of the GDE directly to ambient air, and the CCS anode configuration was changed to the CCM configuration by directly hot-pressing a mixture of IrO₂ catalysts and Nafion ionomer onto the PEM (see Fig. S5 for the modified PSE reactor).

H₂O₂ concentrations were measured using the potassium titanium (IV) oxalate (AR) method with a spectrophotometer at 402 nm (Dr 6000, Hitachi Co., Ltd., Japan)⁴³. The FE, EC, and rate of H₂O₂ production were calculated according to Eqs. 4–6 (see SI S8 for more information).

$$\text{FE}(\%) = \frac{nFcv}{M \times 6 \times 10^7} \times 100\% = \frac{cv}{105751} \times 100\% \quad (4)$$

$$\text{EC} = \frac{10^6 UI}{60cv} = \frac{1.576U}{FE} \quad (5)$$

$$r = \frac{60cv}{1000S} = 0.634j \times FE \quad (6)$$

where n is the electron transfer number for one O₂ molecule reduction to H₂O₂ ($n = 2$), F is the Faraday constant (96,485 C/mol), c is the measured H₂O₂ concentration (mg/L), v is the flow rate (mL/min), M is the molar mass of H₂O₂ (34.01 g/mol), I is the applied current (A), EC is the energy consumption of H₂O₂ production (kWh/kg H₂O₂), U is the cell voltage (V), r is the rate of H₂O₂ production (mg/h/cm²), S is the effective area (cm²).

Analytical methods

The PSE ion exchange capacity was determined using a titration method. Approximately 15 mL of the PSE was placed into an ion exchange column and then treated by 1 M HCl washing. The HCl flow rate and treating time were set to ~5 mL/min and 1 h, which ensured the PSE entirely turned into H⁺-type. Subsequently, the PSE was washed with DI water till the effluent pH to ~7. Next, the external water of the H⁺-type PSE was removed by centrifugation with 2000 rpm for 5 min. Then, about 1.5 g of the H⁺-type PSE was soaked into 100 mL 0.5 M CaCl₂ a conical flask for 2 h. Finally, 25 mL of the solution was moved to another conical flask and then titrated by 0.1 M NaOH with two drops of phenolphthalein being the indicator. The ion exchange capacity Q (meq/g) was calculated using Eq. 7.

$$Q = \frac{4V_{\text{NaOH}}c_{\text{NaOH}}}{m_{\text{PSE}}} \quad (7)$$

where V_{NaOH} and c_{NaOH} are the consumed volume of NaOH, m_{PSE} is the mass of PSE.

Groundwater was collected from the campus of Tsinghua University. The Na, Ca, Mg, As, and Pb in the PSE cell influent and effluent

were analyzed by an ICAP RQplus inductively coupled plasma-mass spectrometry (ThermoFisher Co., Ltd., USA). Total organic carbon was measured with a TOC-V (Shimadzu Co., Ltd., Japan).

The disinfection test was conducted as follows. The mixture of *E. coli* (−7.11 log CFU/mL) and PSE cell effluent (500–10,000 mg/L H₂O₂) was mixed for 15 min. The residual H₂O₂ was then quenched by 10 mM sodium thiosulfate. The samples were diluted and then spread on nutrient agar plates. After 12 h incubation at 37 °C in a dark place, the colonies that formed on the plates were counted.

Characterizations

The Brunauer-Emmett-Teller surface areas of the PSE microspheres were measured with a Nova Station A analyzer (Quantachrome Co., Ltd., USA). The ion exchange capacity of the PSEs was measured using a titration method (see SI text S1 for more detail)^{44,45}. Microscopic images of the PSE microspheres and AEMs were examined by a Su-8220 SEM (Zeiss Merlin Co., Ltd., Germany) with a X-Max EDS (Oxford, UK). The infrared (IR) spectrum of AEMs were collected by an iSSO ATR-IR spectroscopy (Thermo Fisher Co., Ltd., USA).

Calibration of reference electrode and potential scaling

The calibration of the Ag/AgCl reference electrode is based on the potential difference between reference electrode and RHE. The reference electrode and the RHE were simultaneously inserted into a 0.5 M H₂SO₄ solution (1 M H⁺). Subsequently, the open-circuit potential between the two electrodes was measured using an electrochemical workstation. If the open-circuit potential is 0.197 ± 0.005 V, the reference electrode can be considered accurate. Otherwise, the electrolyte inside the reference electrode should be replaced with freshly prepared saturated KCl solution.

All potentials measured against Ag/AgCl was converted to the reversible hydrogen electrode (RHE) scale in this work using Eq. 8.

$$E_{\text{RHE}} = E_{\text{Ag/AgCl}} + 0.197 + 0.0591 \times \text{pH} \quad (8)$$

where E_{RHE} is the potential versus RHE, $E_{\text{Ag/AgCl}}$ is the potential versus Ag/AgCl electrode.

Computational details

To assess the HO₂[−] conductivity of the different AEMs, MD simulation was performed using the LAMMPS program with a hybrid force field (TIP4P-2005 for water and GAFF2 for other molecules). All calculations were performed using isothermal-isobaric ensemble (NPT) or canonical ensemble (NVT), with a temperature of 298.15 K and a pressure of 0.0001 GPa. The timestep and total simulation time were set to 0.1 fs and 10 ps. The average RDF data was collected from the last 5 ps with every frame. For all calculations, 40 hydroperoxide ions, 40λ water molecules (λ is the measured water uptake of AEMs, see SI Table S1 for more detail), and one polymer of AEM that contains 40 monomers is placed in a box. The HO₂[−] conductivity of AEMs is calculated by the Nernst-Einstein equation (Eq. 9)⁴⁶.

$$\sigma = \frac{z^2 D F^2}{RT} \quad (9)$$

where σ is the conductivity (S/m), z is number of ion charge, R is the ideal gas constant (8.314 J/(mol K)), T is the temperature (K), D is the diffusion coefficient (m²/s) calculated according to the Stokes-Einstein equation (Eq. 10).

$$D = \frac{1}{6N_a} \lim_{t \rightarrow \infty} \frac{d}{dt} \sum_{i=1}^{N_a} \langle [r_i(t) - r_i(0)]^2 \rangle \quad (10)$$

where $r_i(t)$ and $r_i(0)$ are the displacement of ion i after and before diffusion time t , N_a is the number of ions.

The calculations of energy, highest occupied molecular orbital (HOMO), lowest unoccupied orbital (LUMO), and Fukui function based on DFT were performed using Gaussian 16 software with a M06-2X/6-311+G(d,p) level and Multiwfn 3.8 program^{47–50}. The visualization was conducted using VMD 1.9.3 software⁵¹. The optimization convergence thresholds were set to 4.5×10^{-4} Ha for the force and 1.8×10^{-3} Ha for the displacement. The spin polarization was considered for all the calculations. For all reactions, the reaction Gibbs free energy is calculated using Eq. 11.

$$\Delta G_{\text{reaction}} = (E + G_{298.15\text{K}})_{\text{total product}} - (E + G_{298.15\text{K}})_{\text{total reactant}} \quad (11)$$

where $\Delta G_{\text{reaction}}$ is the reaction Gibbs free energy, E is the single-point energy at 0 K, and G is the thermodynamic correction at 298.15 K.

The CFD simulation was conducted using Ansys Fluent 2020. The laminar model was employed to predict the hydrodynamics inside the reactor because of the low influent flow rate (1–5 mL/min). A porous media model with an average pore width of 200 μm was used to simulate the PSEs and their gaps.

Data availability

The data supporting the findings of this study are included in the main text and Supplementary information files, and the source data are reported in the Source Data file. Source data are provided with this paper.

References

- Pesterfield, L. The 100 Most important chemical compounds: a reference guide. *J. Chem. Educ.* **86**, 1182.
- Goyal, R., Singh, O., Agrawal, A., Samanta, C. & Sarkar, B. Advantages and limitations of catalytic oxidation with hydrogen peroxide: from bulk chemicals to lab scale process. *Cat. Rev. Sci. Eng.* **64**, 229–285 (2020).
- Yuan, Y. et al. Electrocatalytic ORR-coupled ammoximation for efficient oxime synthesis. *Sci. Adv.* **10**, eado1755 (2024).
- Cui, L. et al. An anti-electrowetting carbon film electrode with self-sustained aeration for industrial H_2O_2 electrosynthesis. *Energy Environ. Sci.* **17**, 655–667 (2024).
- Ciriminna, R., Albanese, L., Meneguzzo, F. & Pagliaro, M. Hydrogen peroxide: a key chemical for today's sustainable development. *ChemSusChem* **9**, 3374–3381 (2016).
- Yang, S. et al. Toward the decentralized electrochemical production of H_2O_2 : a focus on the catalysis. *ACS Catal.* **8**, 4064–4081 (2018).
- Wen, Y. et al. Electrochemical reactors for continuously decentralized H_2O_2 production. *Angew. Chem. Int. Ed. Engl.* **61**, e202205972 (2022).
- Zhao, E. et al. Technoeconomic assessment of electrochemical hydrogen peroxide production with gas diffusion electrodes under scenarios relevant to practical water treatment. *ACS ES&T Eng* **3**, 1800–1812 (2023).
- Xia, C., Xia, Y., Zhu, P., Fan, L. & Wang, H. Direct electrosynthesis of pure aqueous H_2O_2 solutions up to 20% by weight using a solid electrolyte. *Science* **366**, 226–231 (2019).
- Shin, H., Lee, S. & Sung, Y. E. Industrial-scale H_2O_2 electrosynthesis in practical electrochemical cell systems. *Curr. Opin. Electrochem.* **38**, 101224 (2023).
- Sabri Rawah, B., Albloushi, M. & Li, W. Electro-synthesis of pure aqueous H_2O_2 on nitrogen-doped carbon in a solid electrolyte flow cell without using anion exchange membrane. *Chem. Eng. J.* **466**, 143282 (2023).
- Xia, Y. et al. Highly active and selective oxygen reduction to H_2O_2 on boron-doped carbon for high production rates. *Nat. Commun.* **12**, 4225 (2021).
- Zhao, E., Wang, S., Yu, G. & Wang, Y. Insight into the deterioration mechanism of gas diffusion electrode during long-term electro-synthesis of hydrogen peroxide under industrially relevant current densities. *Electrochim. Acta* **502**, 144835 (2024).
- Zhang, H. et al. Integrating H_2O_2 generation from electrochemical oxygen reduction with the selective oxidation of organics in a dual-membrane reactor. *Chem. Eng. J.* **428**, 131534 (2022).
- Zhang, X. et al. Electrochemical oxygen reduction to hydrogen peroxide at practical rates in strong acidic media. *Nat. Commun.* **13**, 2880 (2022).
- Klumpen, C., Godrich, S., Papastavrou, G. & Senker, J. Water mediated proton conduction in a sulfonated microporous organic polymer. *Chem. Commun.* **53**, 7592–7595 (2017).
- Liu, M. et al. Three-dimensional protonic conductivity in porous organic cage solids. *Nat. Commun.* **7**, 12750 (2016).
- Grew, K. N. & Chiu, W. K. S. A dusty fluid model for predicting hydroxyl anion conductivity in alkaline anion exchange membranes. *J. Electrochem. Soc.* **157**, B327–B337 (2010).
- Liu, Z. et al. The effect of membrane on an alkaline water electrolyzer. *Int. J. Hydrogen Energy* **42**, 29661–29665 (2017).
- Müller, F., Ferreira, C. A., Azambuja, D. S., Alemán, C. & Armelin, E. Measuring the proton conductivity of ion-exchange membranes using electrochemical impedance spectroscopy and through-plane cell. *J. Phys. Chem. B* **118**, 1102–1112 (2014).
- Swenson, J. & Börjesson, L. Correlation between free volume and ionic conductivity in fast ion conducting glasses. *Phys. Rev. Lett.* **77**, 3569–3572 (1996).
- Christie, A. M., Lilley, S. J., Staunton, E., Andreev, Y. G. & Bruce, P. G. Increasing the conductivity of crystalline polymer electrolytes. *Nature* **433**, 50–53 (2005).
- Liu, Z., Sajjad, S. D., Gao, Y., Kaczur, J. & Masel, R. An alkaline water electrolyzer with Sustainion™ membranes: 1 A/cm² at 1.9 V with base metal catalysts. *ECS Trans* **77**, 71 (2017).
- Sajjad, S. D., Gao, Y., Liu, Z., Yang, H. & Masel, R. Tunable-high performance Sustainion™ anion exchange membranes for electrochemical applications. *ECS Trans* **77**, 1653 (2017).
- Rai, V. et al. Serum-based diagnostic prediction of oral submucous fibrosis using FTIR spectrometry. *Spectrochim. Acta Part A: Mol. and Biomol. Spectrosc.* **189**, 322–329 (2018).
- Rozenberg, M., Lansky, S., Shoham, Y. & Shoham, G. Spectroscopic FTIR and NMR study of the interactions of sugars with proteins. *Spectrochim. Acta A* **222**, 116861 (2019).
- Baasov, T., Friedman, N. & Sheves, M. Factors affecting the C:N stretching in protonated retinal Schiff base: a model study for bacteriorhodopsin and visual pigments. *Biochemistry* **26**, 3210–3217 (1987).
- Ji, S., Jiang, T., Xu, K. & Li, S. FTIR study of the adsorption of water on ultradispersed diamond powder surface. *Appl. Surf. Sci.* **133**, 231–238 (1998).
- Ludvigsson, M., Lindgren, J. & Tegenfeldt, J. FTIR study of water in cast Nafion films. *Electrochim. Acta* **45**, 2267–2271 (2000).
- Busca, G., Guidetti, R. & Lorenzelli, V. Fourier-transform infrared study of the surface properties of cobalt oxides. *J. Chem. Soc., Faraday Trans.* **86**, 989–994 (1990).
- Nobukawa, T. et al. In-situ observation of reaction intermediate in the selective catalytic reduction of N_2O with CH_4 over Fe ion-exchanged BEA zeolite catalyst for the elucidation of its reaction mechanism using FTIR. *J. Phys. Chem. B* **108**, 4071–4079 (2004).
- Poletto, M., Zattera, A. J. & Santana, R. M. C. Structural differences between wood species: evidence from chemical composition, FTIR spectroscopy, and thermogravimetric analysis. *J. Appl. Polym. Sci.* **126**, 337–344 (2012).
- Majid, S. R. & Arof, A. K. FTIR studies of chitosan-orthophosphoric acid-ammonium nitrate-aluminosilicate polymer electrolyte. *Mol. Cryst. Liq. Cryst.* **484**, 483–492 (2008).

34. Marron, E. L., Mitch, W. A., Gunten, U. V. & Sedlak, D. L. A tale of two treatments: the multiple barrier approach to removing chemical contaminants during potable water reuse. *Acc. Chem. Res.* **52**, 615–622 (2019).
35. Barazesh, J. M., Hennebel, T., Jasper, J. T. & Sedlak, D. L. Modular advanced oxidation process enabled by cathodic hydrogen peroxide production. *Energy Environ. Sci.* **49**, 7391–7399 (2015).
36. Zhang, Q. et al. Highly efficient electrosynthesis of hydrogen peroxide on a superhydrophobic three-phase interface by natural air diffusion. *Nat. Commun.* **11**, 1731 (2020).
37. Martinez-Huitle, C. A., Rodrigo, M. A., Sires, I. & Scialdone, O. Single and coupled electrochemical processes and reactors for the abatement of organic water pollutants: a critical review. *Chem. Rev.* **115**, 13362–13407 (2015).
38. Pan, L. et al. Dead-zone-compensated design as general method of flow field optimization for redox flow batteries. *Proc. Natl. Acad. Sci. USA.* **120**, e2305572120 (2023).
39. von Sonntag, C. & von Gunten, U. Chemistry of ozone in water and wastewater treatment: from basic principles to applications (IWA Publishing, 2012).
40. Lin, Z. et al. Atomic Co decorated free-standing graphene electrode assembly for efficient hydrogen peroxide production in acid. *Energy Environ. Sci.* **15**, 1172–1182 (2022).
41. Chen, S. et al. Identification of the highly active Co–N₄ coordination motif for selective oxygen reduction to hydrogen peroxide. *J. Am. Chem. Soc.* **144**, 14505–14516 (2022).
42. Chen, S. et al. Chemical identification of catalytically active sites on oxygen-doped carbon nanosheet to decipher the high activity for electro-synthesis hydrogen peroxide. *Angew. Chem. Int. Ed. Engl.* **133**, 16743–16750 (2021).
43. Sellers, R. M. Spectrophotometric determination of hydrogen peroxide using potassium titanium(IV) oxalate. *Analyst* **105**, 950–954 (1980).
44. Gregor, H. P. & Bregman, J. I. Characterization of ion exchange resins. I. Acidity and number of constituent cation exchange groups 1,2. *J. Am. Chem. Soc.* **70**, 2370–2373 (1948).
45. Topp, N. E. & Pepper, K. W. 690. Properties of ion-exchange resins in relation to their structure. Part I. Titration curves. *J. Chem. Soc.* 3299–3303 (1949).
46. Takaba, H., Hisabe, T., Shimizu, T. & Alam, M. K. Molecular modeling of OH[−] transport in poly(arylene ether sulfone ketone)s containing quaternized ammonio-substituted fluorenyl groups as anion exchange membranes. *J. Membr. Sci.* **522**, 237–244 (2017).
47. Frisch, M. J. et al. Gaussian 16 Rev. A.03 (Gaussian, Inc., Wallingford, CT, 2016).
48. Lu, T. & Chen, F. Multiwfn: a multifunctional wavefunction analyzer. *J. Comput. Chem.* **33**, 580–592 (2012).
49. Zhao, Y. & Truhlar, D. G. The M06 suite of density functionals for main group thermochemistry, thermochemical kinetics, noncovalent interactions, excited states, and transition elements: two new functionals and systematic testing of four M06-class functionals and 12 other functionals. *Theor. Chem. Acc.* **120**, 215–241 (2008).
50. Krishnan, R., Binkley, J. S., Seeger, R. & Pople, J. A. Self-consistent molecular orbital methods. XX. A basis set for correlated wave functions. *J. Chem. Phys.* **72**, 650–654 (2008).
51. Humphrey, W., Dalke, A. & Schulten, K. VMD: visual molecular dynamics. *J. Mol. Graph.* **14**, 33–38 (1996).
52. Liu, C. et al. Heterogeneous molecular Co–N–C catalysts for efficient electrochemical H₂O₂ synthesis. *Energy Environ. Sci.* **16**, 446–459 (2023).
53. Dong, K. et al. Conductive two-dimensional magnesium metal–organic frameworks for high-efficiency O₂ electroreduction to H₂O₂. *ACS Catal.* **12**, 6092–6099 (2022).
54. Xu, J. et al. Organic wastewater treatment by a single-atom catalyst and electrolytically produced H₂O₂. *Nat. Sustain.* **4**, 233–241 (2020).
55. Li, Y. et al. Evaluation of the technoeconomic feasibility of electrochemical hydrogen peroxide production for decentralized water treatment. *Front. Environ. Sci. Eng.* **15**, 15 (2020).

Acknowledgements

This work was supported by the National Key Research and Development Program (2022YFC3203005 to Y.W.), Tsinghua-Toyota Joint Research Fund (20223930086 to Y.W.), and Jiangsu Provincial Natural Science Foundation (BK20210104 to G.X.).

Author contributions

Conceptualization: E.Z.Z., Y.Y.Z., Y.J.W.; data curation: E.Z.Z., Y.Y.Z.; M.D., D.F.T., and C.F.D. calculation: E.Z.Z.; methodology: E.Z.Z., J.H.Z., G.S.X., Y.J.W.; funding acquisition: G.Y., Y.J.W.; writing—original draft, review & editing: E.Z.Z., Y.J.W.

Competing interests

The authors declare no competing interests.

Additional information

Supplementary information The online version contains supplementary material available at <https://doi.org/10.1038/s41467-025-58385-2>.

Correspondence and requests for materials should be addressed to Yujue Wang.

Peer review information *Nature Communications* thanks Christian Durante, and the other, anonymous, reviewer(s) for their contribution to the peer review of this work. A peer review file is available.

Reprints and permissions information is available at <http://www.nature.com/reprints>

Publisher's note Springer Nature remains neutral with regard to jurisdictional claims in published maps and institutional affiliations.

Open Access This article is licensed under a Creative Commons Attribution-NonCommercial-NoDerivatives 4.0 International License, which permits any non-commercial use, sharing, distribution and reproduction in any medium or format, as long as you give appropriate credit to the original author(s) and the source, provide a link to the Creative Commons licence, and indicate if you modified the licensed material. You do not have permission under this licence to share adapted material derived from this article or parts of it. The images or other third party material in this article are included in the article's Creative Commons licence, unless indicated otherwise in a credit line to the material. If material is not included in the article's Creative Commons licence and your intended use is not permitted by statutory regulation or exceeds the permitted use, you will need to obtain permission directly from the copyright holder. To view a copy of this licence, visit <http://creativecommons.org/licenses/by-nc-nd/4.0/>.

© The Author(s) 2025